Supporting Information

Ultrabright room-temperature sub-nanosecond emission from single nitrogen-vacancy centers coupled to nano-patch antennas

Simeon I. Bogdanov[†,‡]*, Mikhail Y. Shalaginov[†,‡], Alexei S. Lagutchev[†,‡], Chin-Cheng Chiang[†,‡], Deesha Shah[†,‡], Alexandr S. Baburin[§,k], Ilya A. Ryzhikov[§,¶], Ilya A. Rodionov[§,k], Alexander V. Kildishev[†,‡], Alexandra Boltasseva[†,‡] and Vladimir M. Shalaev[†,‡]

[†]School of Electrical & Computer Engineering and Birck Nanotechnology Center, Purdue University, West Lafayette, IN 47907, USA

[‡]Purdue Quantum Center, Purdue University, West Lafayette, IN 47907, USA

[§]FMNS REC, Bauman Moscow State Technical University, Moscow, 105005, Russia

[k]Dukhov Research Institute of Automatics, Moscow, 127055, Russia

[¶]Institute for Theoretical and Applied Electromagnetics RAS, Moscow, 125412, Russia

*E-mail: sbogdan@purdue.edu

I. Substrate fabrication

a. Ag substrate deposition

The polycrystalline silver substrate was deposited using an e-beam evaporator (Leybold) at a base pressure of $2 \cdot 10^{-6}$ Torr. First, an adhesion layer of Ti (10 nm) was deposited on <100> Si substrate, then a 50 nm layer of Ag. The sample spent 10-15 min in air before the deposition of the spacer layer. A control sample underwent the same deposition procedure and was then characterized by ellipsometry to retrieve the optical properties of the silver substrate. The dielectric permittivity data is plotted on Figure S1.
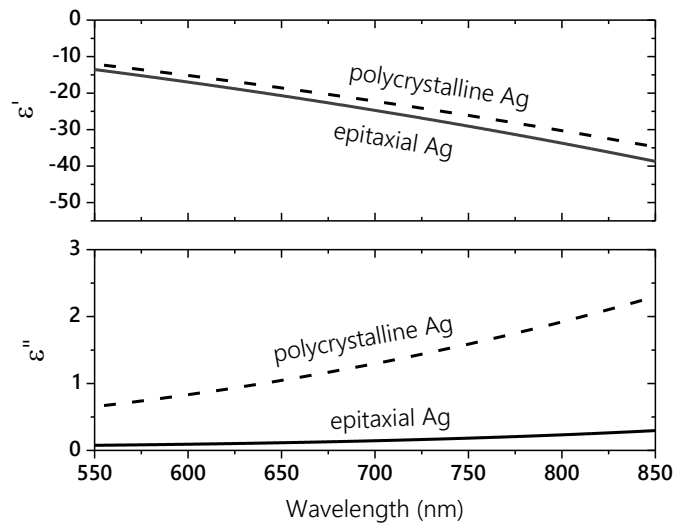

Figure S1. Dielectric permittivity constants of polycrystalline and epitaxial Ag obtained from ellipsometry measurements.

The epitaxial silver substrate was deposited using an e-beam evaporator (Angstrom Engineering) at a base pressure of $3 \cdot 10^{-8}$ Torr. 35 nm layer of Ag was deposited on <111> Si

substrate without any adhesion layer. The epitaxial silver samples spent 2 weeks in air before NPA fabrication and measurements. A control sample underwent the same deposition procedure and was then characterized by ellipsometry to retrieve the optical properties of the epitaxial silver substrate. The dielectric permittivity data is plotted in Figure S1. The wavelength used in simulations is 640 nm and the dielectric permittivity of the substrate at this wavelength is $\varepsilon = -19.93 + i0.11$.

b. Spacer deposition

The spacer layer was formed by deposition of individual self-assembled monolayers following a standard procedure described in detail elsewhere[1,2] and shortly summarized as follows. First, the silver substrate was dipped into a 0.003 monomol/L poly-allyalamine (PAH) solution with 1 M of NaCl for 5 min, rinsed with water, then immersed into a 1M NaCl solution for 30 seconds. The procedure was then repeated for the deposition of a polystyrene sulfonate layer (PSS) and the final PAH layer. The compounded thickness of three monolayers was 6 ± 2 nm as determined by ellipsometry.

II. Setup efficiency

Setup efficiency is defined as the fraction of photons emitted within the objective's collection angle that are registered by the detector. A collimated 638 nm laser beam was coupled into the BD objective, and we measured its power at the sample position using a sensitive power meter (PM16-130, Thorlabs). Then, a mirror with 95% nominal reflectivity was installed at the sample position and the reflected laser light was registered by the single-photon detector that was used in the saturation curve measurements (SPCM-AQRH, Excelitas). We then divided the measured photon count rate at the single-photon detector by the photon flux measured by the power meter at the sample location. The measurement yielded a setup efficiency of $14 \pm 1\%$.

We checked this measurement by numerically compounding nominal optical losses at all the elements in the fluorescence path. The losses include the following components: objective transmission, reflections at the mirrors, dichroic mirror transmission, transmission of confocal telescope, consisting of two lenses and one pinhole, transmission of detector's lens and detector quantum efficiency. Accounting for these losses, we obtain an "ideal" setup efficiency of 20 ± 1%. The measured value is in good agreement with our estimate. The discrepancy may be due to the imperfections in the microscope alignment, optical aberrations and accidental dust particles on the optical components.

III.   Simulations of emission properties

The numerical electromagnetic calculations were performed using finite-element time-domain method with a commercial solver COMSOL 5.3, Wave Optics Module. Optical permittivity data of epitaxial silver film obtained from the variable angle spectroscopic ellipsometry measurements (see **Figure S1**) were used to simulate the emission of the NV-NPA. The simulation domain represents a cube with a side of 1.8 μm or 2.4 μm for NVNPA or NVG configurations, respectively. In both cases the domains were truncated with a standard 400-nm-thick PML layer. The dipole emitter at 640-nm-wavelength was introduced as a volume current density coherently oscillating inside a 2-nm-radius sphere. The total decay rate γ is calculated as the surface integral of total power flow **P** through a 3-nm-radius spherical surface Ω_{in} encapsulating the emitting dipole and situated entirely within the nanodiamond volume (see **Figure S2**): $\gamma \propto \int_{\Omega_{in}} \mathbf{P} \cdot \mathbf{dS}$. The loss rate γ^{loss} is calculated as the total work performed by the electric field on the free charges in the metal regions occupying the volume V_m :

$$\gamma^{loss} = \int_{V_m} \mathbf{j} \cdot \mathbf{E} dV .$$

All the numerically obtained power flows are normalized by the power dissipated by an NV center in bulk diamond corresponding to a known bulk decay rate of $\gamma^{bulk} = (12.8\ \text{ns})^{-1}$. The simulated rates can therefore be expressed in units of ns^{-1}. Finally, the collection efficiency η^{col} is calculated as the ratio of the far-field electric fields squared integrated over a spherical outer surface Ω_{out} (0.7-µm-radius sphere for NV-NPA and 1-µm for NVG) and the portion of that surface Ω_{col} corresponding to the collection solid angle of the relevant objective: altitude angles of 64° (0.9 NA) and 79.6° (1.49 NA) for NV-NPA and NV-G, respectively. The far-field electric fields were calculated using a standard near-field to far-field transformation[S3].
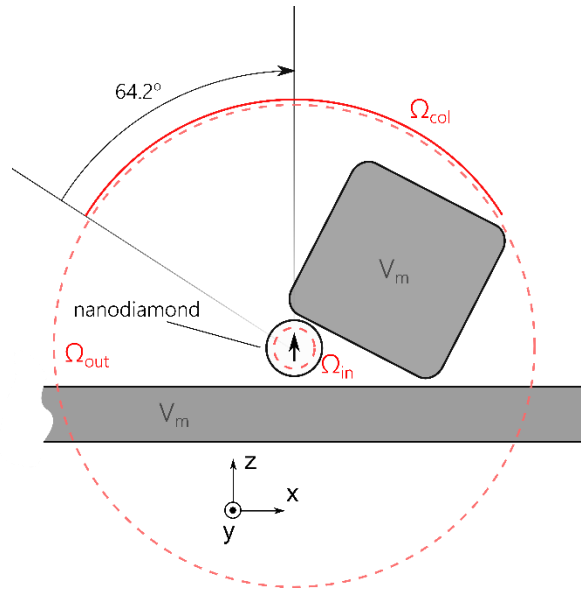

Figure S2. Schematic illustration of integration volumes and surfaces used for simulating efficiency parameters of the NV-NPA.

The summary of numerically obtained quantities γ, γ^{loss}, η^{col} for basis dipole orientations in NV-NPA and NV-G cases are presented in **Table S1**. The quantity γ^{ff} used in the main text represents the difference $\gamma - \gamma^{loss}$.

Table S1. Summary of simulated rates of dipole emission, photon loss to metal as well as collection efficiency.

Emitter and orientation	γ (ns^{-1})	γ^{loss} (ns^{-1})	η^{col} (%)
NV in NPA (z-dipole)	0.39^{-1}	16.8^{-1}	45
NV in NPA (x-dipole)	516^{-1}	911^{-1}	30
NV in NPA (y-dipole)	5.17^{-1}	207^{-1}	46
NV-G (z-dipole)	84.5^{-1}	0	85
NV-G (x-dipole)	147^{-1}	0	82

We performed an estimate of the collection efficiency for the NV-G source using semi-analytical calculations. For a single dipole emitter with in-plane (x,y) or perpendicular (z) orientation placed at a distance h above oil/glass planar interface, the corresponding η^{col} can be calculated using dyadic Green function formalism[4].

$$\eta^{col} = \int_{\varepsilon_{sup}^{1/2}}^{\infty} p_\kappa d\kappa \Bigg/ 1 + \int_{0}^{\infty} p_\kappa d\kappa \,, \qquad \text{S(1)}$$

where depending on dipole orientation, wave-vector density is expressed as

$$p_\kappa^{(z)} = \frac{3}{2}\frac{1}{\varepsilon_{sup}^{3/2}}\text{Re}\left\{\frac{\kappa^3}{\kappa_{z,sup}(\kappa)}r^p(\kappa)e^{2ik_0\kappa_{z,sup}(\kappa)h}\right\}, \qquad \text{S(2)}$$

$$p_\kappa^{(x,y)} = \frac{3}{4}\frac{1}{\varepsilon_{sup}^{1/2}}\text{Re}\left\{\frac{\kappa}{\kappa_{z,sup}(\kappa)}\left[r^s(\kappa)-\frac{\kappa_{z,sup}^2(\kappa)}{\varepsilon_{sup}}r^p(\kappa)\right]e^{2ik_0\kappa_{z,sup}(\kappa)h}\right\}. \qquad \text{S(3)}$$

In equations S(1) - S(3), $\kappa = k_{x,y}/k_0$; $\kappa_{z,\text{sup}}(\kappa) = k_{z,\text{sup}}/k_0 = \left(\varepsilon_{\text{sup}} - \kappa^2\right)^{1/2}$; ε_{sup}, ε_{sub} are superstrate and substrate relative permittivities, i. e. $\varepsilon_{\text{sup}} = 2.3$ and $\varepsilon_{\text{sub}} = 2.16$; r^p and r^s are conventional Fresnel coefficients: $r^p = \dfrac{\varepsilon_{\text{sub}}\kappa_{z,\text{sup}} - \varepsilon_{\text{sup}}\kappa_{z,\text{sub}}}{\varepsilon_{\text{sub}}\kappa_{z,\text{sup}} + \varepsilon_{\text{sup}}\kappa_{z,\text{sub}}}$, $r^s = \dfrac{\kappa_{z,\text{sup}} - \kappa_{z,\text{sub}}}{\kappa_{z,\text{sup}} + \kappa_{z,\text{sub}}}$. The integrals were numerically evaluated using an adaptive Gauss–Kronrod quadrature method[S5]. Semi-analytically calculated values of η^{col} are 82% and 85% for (x,y) and z dipole orientations, correspondingly, which agrees well with the values obtained from numerical simulations.

IV. Statistics of reference emitters: single NVs on coverslip glass

In the control experiment, we have measured the photophysical properties of 14 nanodiamonds containing single NVs which were dispersed on a coverslip glass substrate. The summary of the measurement results is shown in **Figure S3**. The spread in fluorescence lifetime arise from two separate causes. First, the radiative decay rates depend on the dipole orientation (see section III). Second, the variations in quantum yield, which are known to be wide in commercial nanodiamonds[S6] (see section VI for more details on estimating quantum yield), also contribute to the observed lifetime. The spread in saturation intensity is due to variations in dipole orientation, which affects the radiative decay rate. The saturating pump intensities are the most broadly distributed because they are affected by both the fluorescence lifetime and random dipole orientations with respect to the pump polarization direction. Black arrows indicate the values corresponding to the brightest emitter chosen as the reference NVG source described in the main text.
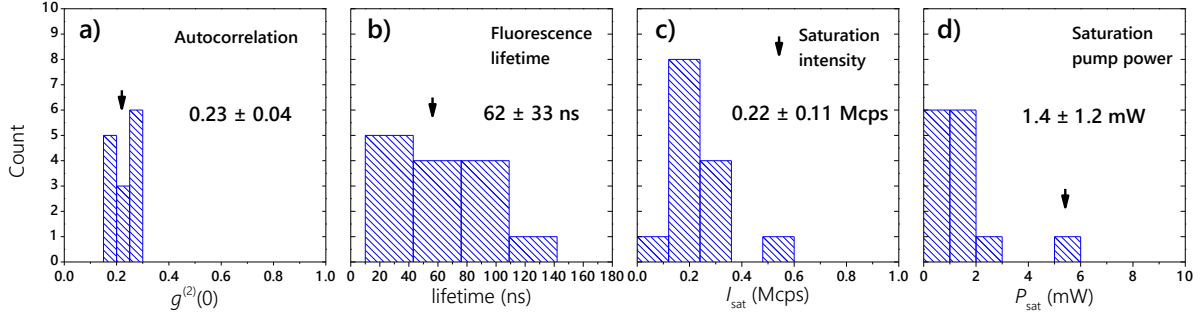
Figure S3. Statistical distributions of the photophysical properties of NV centers in nanodiamonds dispersed on glass coverslip and characterized with an oil objective with NA = 1.49 in the TIRF configuration. (a) Antibunching at zero delay in the autocorrelation function. (b) Fluorescence lifetime. (c) Saturated emission intensity. (d) Saturating pump power. Solid lines are gamma distribution fits to the measured data.

V.   NV quantum yield

We estimate the NV quantum yield from measurements of fluorescence lifetime. This method relies on several assumptions. First, we assume the NV's intrinsic lifetime in bulk diamond to be constant $\tau_{\text{bulk, i}} = 12.8 \text{ ns}$. Second, we assume that the relation between the lifetime of an emitter in bulk diamond and emitter in a nanodiamond surrounded by vacuum obeys the following analytical expression[S7]:

$$\frac{\tau_{\text{ND, 0}}}{\tau_{\text{bulk, 0}}} = n\left(\frac{n^2 + 2}{3}\right)^2 \approx 17 \qquad \text{S(4)}$$

For the emitters in nanodiamonds on glass substrate, an additional lifetime shortening is predicted by our numerical simulations: $\dfrac{\tau_{\text{g, 0}}}{\tau_{\text{ND, 0}}} \approx 0.7$. Here, the index 0 refers to the radiative lifetime values, not accounting for the non-radiative decay processes. As all the nanodiamonds in

8

our study are highly subwavelength, the variations in their sizes and shapes are not expected to influence these lifetime values. Therefore, we can deduce the quantum yield of our NVs by comparing the measured lifetime on glass to the theoretical lifetime $\tau_{g,0} \approx 155$ ns computed from the considerations above. Using this method, we obtain $QY = 40 \pm 20\%$. We further note that the NV center can exist in two different charge states (NV^0 and NV^-) with somewhat different intrinsic lifetimes[S8]. Therefore, the quantum efficiency estimates may be influenced by equilibrium charge population of the NV center, which nevertheless remains predominantly NV^- at excitation wavelengths employed in our experiment[S9].

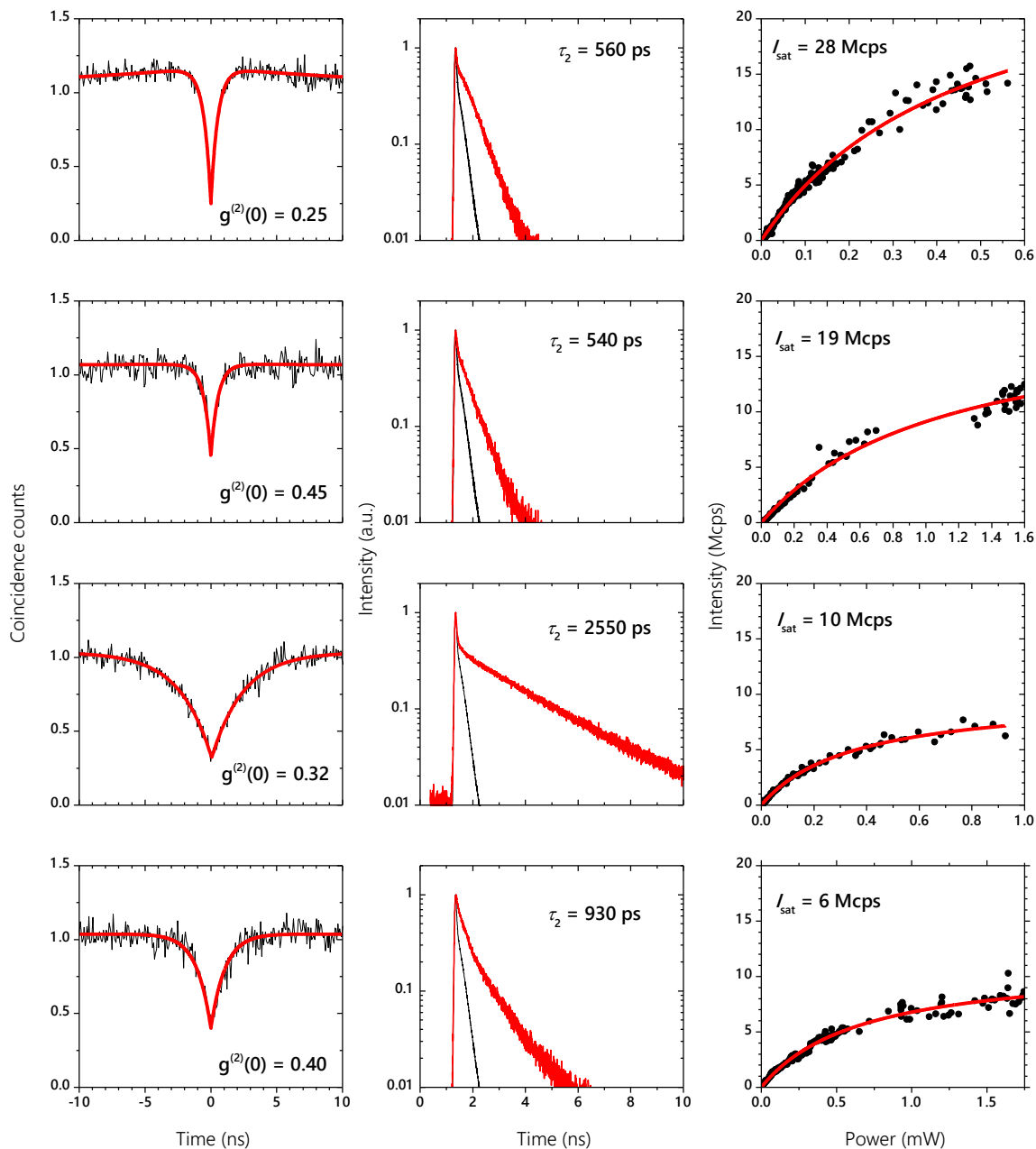## VI.   Additional emitters coupled to NPAs

Figure S4. Autocorrelation curves (left column), fluorescence decays (middle column) and saturation curves (right column) for three NV center emitters enhanced by NPA structures assembled on epitaxial silver substrate.

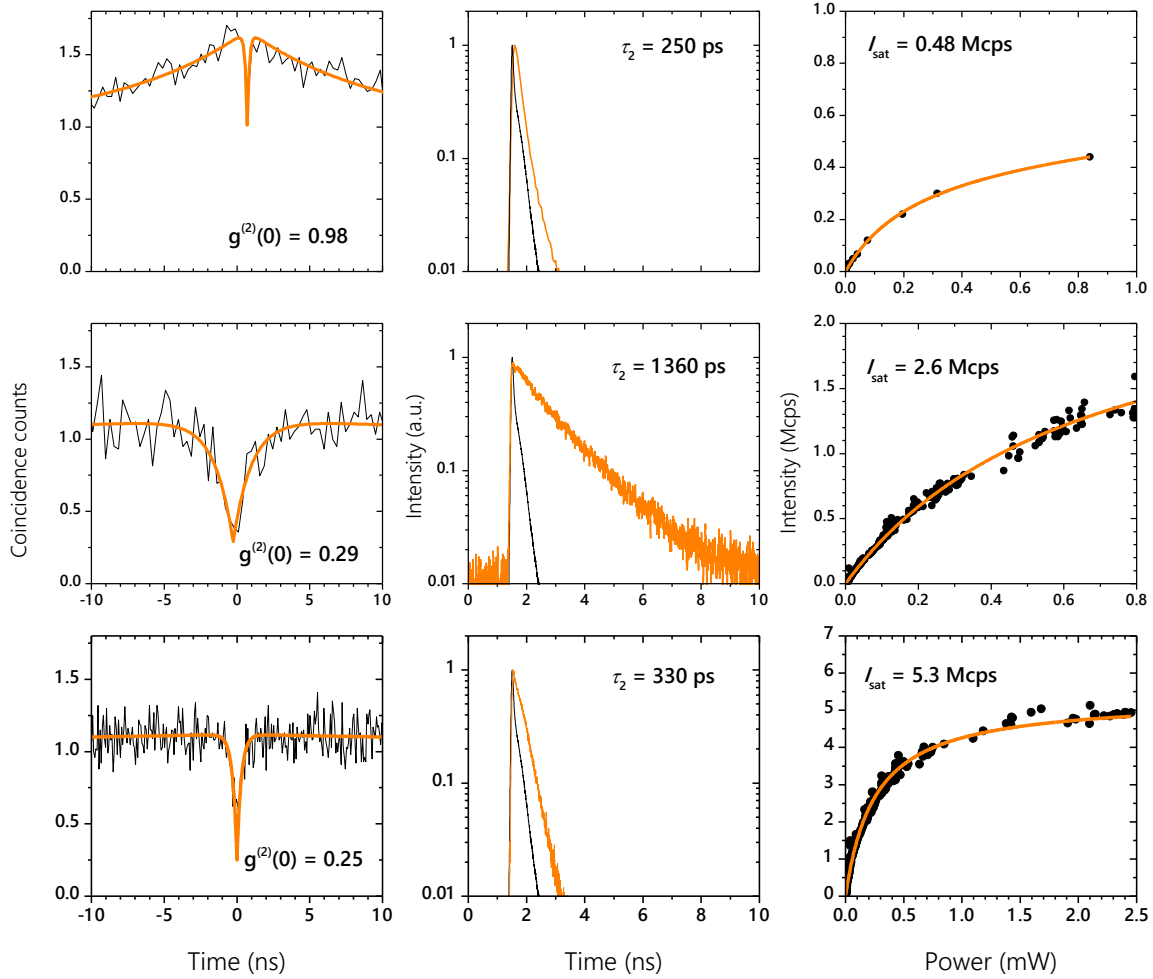# VII. Additional emitters coupled to NPAs on polycrystalline silver substrate

Figure S5. Autocorrelation curves (left column), fluorescence decays (middle column) and saturation curves (right column) for three NPA-enhanced NVs, similar to the NV-NPA emitter described in the main text, assembled on polycrystalline silver substrate.

References

(S1)   Moreau, A.; Ciracì, C.; Mock, J. J.; Hill, R. T.; Wang, Q.; Wiley, B. J.; Chilkoti, A.; Smith, D. R. *Nature* **2012**, 492, 86–89.

(S2)   Akselrod, G. M.; Argyropoulos, C.; Hoang, T. B.; Ciracì, C.; Fang, C.; Huang, J.; Smith, D. R.; Mikkelsen, M. H. *Nat. Photonics* **2014**, 8, 835–840.

(S3)   Stratton, J. A. John Wiley & Sons, Inc.: Hoboken, NJ, USA, 2015.

(S4)   Novotny, L.; Hecht, B. Cambridge University Press: Cambridge, 2006.

(S5)   Shampine, L. F. *J. Comput. Appl. Math.* **2008**, 211, 131–140.

(S6)   Mohtashami, A.; Femius Koenderink, A. *New J. Phys.* **2013**, 15.

(S7)   Greffet, J.-J.; Hugonin, J.-P.; Besbes, M.; Lai, N. D.; Treussart, F.; Roch, J.-F. .

(S8)   Liaugaudas, G.; Davies, G.; Suhling, K.; Khan, R. U. A.; Evans, D. J. F. *J. Phys. Condens. Matter* **2012**, 24, 435503.

(S9)   Aslam, N.; Waldherr, G.; Neumann, P.; Jelezko, F.; Wrachtrup, J. *New J. Phys.* **2013**, 15.